BASIC SCIENCE

Nanomedicine: Nanotechnology, Biology, and Medicine
9 (2013) 795–805

Research Article

nanomedjournal.com

Matrigel alters the pathophysiology of orthotopic human breast adenocarcinoma xenografts with implications for nanomedicine evaluation

Adam J. Shuhendler[a], Preethy Prasad[a], Ping Cai[a], Kelvin K.W. Hui[a], Jeffrey T. Henderson[a], Andrew M. Rauth[b,c], Xiao Yu Wu[a,*]

[a]*Department of Pharmaceutical Sciences, Leslie Dan Faculty of Pharmacy, University of Toronto, Toronto, Ontario, Canada*
[b]*Department of Medical Biophysics, University of Toronto, Toronto, Ontario, Canada*
[c]*Ontario Cancer Institute, Princess Margaret Hospital, University Health Network, Toronto, Ontario, Canada*

Received 10 August 2012; accepted 26 January 2013

Abstract

Matrigel, a mouse sarcoma-derived basement membrane protein mixture, is frequently used to facilitate human tumor xenograft growth in rodents. Despite its known effects on tumor growth and metastasis, its impact on tumor pathophysiology and preclinical evaluation of nanomedicines in tumor xenografts has not been reported previously. Herein bilateral MDA435 tumors were established orthotopically with (Mat+) or without (Mat−) co-injection of Matrigel. Tumor perfusion, morphology and nanoparticle retention were evaluated. As compared to Mat− tumors, Mat+tumors exhibited enhanced vascular perfusion and lymphatic flow, greater blood vessel and lymphatic growth within the tumor core, and more deformation and collapse of lymphatics in tumor-associated lymph nodes. These changes were accompanied by reduced nanoparticle retention in Mat+tumors. The results suggest that Matrigel is not a passive medium for tumor growth, but rather significantly alters long-term tumor architecture. These findings have significant implications for the evaluation of therapeutic nanomedicine in xenograft mouse models.

From the Clinical Editor: Matrigel is utilized in facilitating human tumor xenograft growth in rodents. The authors demonstrate that Matrigel is not a passive medium for tumor growth; instead it significantly alters long-term tumor architecture, with major implications in the evaluation of therapeutic nanomedicine in xenograft mouse models.

Key words: Matrigel; Altered pathophysiology; Orthotopic breast adenocarcinoma xenografts; Enhanced tumor perfusion; Lymphangiogenesis; Nanoparticle retention

Xenograft models of solid human tumors propagated in immunodeficient mice are an indispensable element of all aspects of modern cancer research, including the evaluation of nanoparticulate drug delivery systems. However some established human tumor cell lines, as well as primary human tumor biopsy cells are difficult to grow in murine models. By suspending such cells in a basement membrane extract derived from Engelbreth-Holm-Swarm mouse sarcoma (Matrigel), the *in vivo* tumor growth rate of a variety of tumors has been shown to be markedly enhanced, as is the invasiveness of resulting tumors.[1–5] Matrigel treatment can also exacerbate tumor drug resistance phenotypes *in vitro*,[4] and promote progenitor cell phenotypes in luminal cells.[6] None of these tumor-enhancing effects are observed upon co-incubation of tumor cells with factors such as type I collagen alone.[2] This is perhaps not surprising since Matrigel is composed of a mixture of basement membrane components, including laminin, type IV collagen, glycosaminoglycans such as heparan sulfate, proteoglycans, and growth factors such as transforming growth factor-β and platelet derived growth factor.[1–3] As such, co-incubation of a variety of tumor cells with Matrigel has become commonplace in a number of *in vitro* and *in vivo* cellular analyses.

The use of nanoparticles as drug delivery systems to enhance the clinical efficacy of cancer chemotherapeutics has been well

The authors gratefully acknowledge the grant from the Canadian Breast Cancer Foundation – Ontario Region (GRANT #300347), Graduate Scholarship from National Sciences and Engineering Research Council of Canada to A.S. and Ontario Graduate Scholarship to P.P.

Conflict of Interest: The authors have no conflicts of interests.

*Corresponding author: Department of Pharmaceutical Sciences, Lesley Dan Faculty of Pharmacy, University of Toronto, Toronto, Ontario, Canada M5S 3M2.

E-mail address: xywu@phm.utoronto.ca (X.Y. Wu).

1549-9634/$ – see front matter © 2013 Elsevier Inc. All rights reserved.
http://dx.doi.org/10.1016/j.nano.2013.01.005

established in both the pre-clinical and clinical settings.[7] One of the founding principles in the development of these systems is the Enhanced Permeability and Retention (EPR) effect.[8,9] The EPR effect results from the interplay of abnormal tumor vasculature and lymphatics that leads to the passive and selective targeting of tumor tissue by nanoparticles. Enhanced permeability is an effect of active angiogenesis resulting in high vascular density and defective vascular architecture in tumors, which facilitates nanoparticle extravasation.[9] The enhanced retention in contrast is attributable to the impaired tumor-associated lymphatic physiology resulting in a reduced clearance of nanoparticles from the tumor.[8–10]

Although it was reported that tumors grown with and without Matrigel do not exhibit any overt histological or morphological differences in standard analyses,[2,11] it has been shown that the injection of unsupplemented Matrigel, even in growth factor-depleted form, significantly enhances the recruitment of endothelial cells and formation of neovasculature within the myocardium.[12,13] It is therefore conceivable that Matrigel may alter the extracellular environment of developing tumors such that blood flow within the tumor may subsequently impact interstitial fluid convective flow and lymphatic drainage of anti-cancer agents such as nanoparticles. However the effects of Matrigel on tumor physiology have not been previously investigated in detail. To this end, we have examined herein, for the first time, the effect of Matrigel on the physiology of tumor and tumor-associated tissue as it relates to nanoparticle uptake and retention. To mechanistically evaluate the effects of Matrigel on nanomedicine performance in an orthotopic nude mouse model of human MDA435 breast adenocarcinoma, tumors were inoculated bilaterally in each mouse on one side with cells suspended in Matrigel-free growth medium (Mat−) and on the other in Matrigel-containing growth medium (Mat+). The perfusion and morphology of tumor vasculature and lymphatics, as well as nanoparticle retention in tumor tissue were evaluated using contrast-enhanced ultrasound, fluorescent imaging, and immunohistochemical analysis.

Methods

Chemicals and reagents

Eicosanoic acid, poly(ethylene oxide)-40-stearate (Myrj 52), poly(ethylene glycol)-100-stearate (Myrj 56), lead oxide, selenium, trioctylphosphine, oleic acid, octadecene, hexanes, methanol, ethanol, chloroform, octanoic acid, cupric acetate, butanol, acetyl chloride, Geneticin© (G418), calcium phosphate, and indocyanine green were purchased from Sigma-Aldrich Inc. (Oakville, Ontario, Canada) and used without further purification. Pluronic F-68 was purchased from BASF (Mississauga, Ontario, Canada). Chloroform-d was purchased from Cambridge Isotope Laboratories Inc. (Andover, MA, USA). BD Matrigel™ was purchased from BD Biosciences (Mississauga, Ontario, Canada). Alpha minimal essential medium (α-MEM) was purchased from the Media Lab at Princess Margaret Hospital (Toronto, Ontario, Canada), and trypsin and fetal calf serum were purchased from Invitrogen Canada Inc. (Burlington, Ontario, Canada). Human breast cancer MDA435 cells were purchased from ATCC (Manassas, VA, USA). Nude mice (NCR-NU-F) were purchased from Taconic Inc. (Hudson, NY, USA).

Formulation of quantum dot-loaded fatty ester nanoparticles (QD-FEN)

Fatty esters were synthesized as previously reported,[14] and the structure was confirmed in solution with chloroform-d by standard ^{1}H- and ^{13}C-NMR performed on a Varian Mercury 300 MHz instrument (Agilent Technologies Inc. Santa Clara, CA, USA). PbSe quantum dots were synthesized according to previously published methods.[15] The fluorescence spectra of the PbSe QDs were recorded on an Ocean Optics spectrofluorimeter (Ocean Optics, Dunedin, FL, USA). QD-FEN were prepared from synthesized fatty ester and PbSe QDs as previously described.[16,17] Particle size and zeta potential were measured on a Nicomp 380 Zetasizer by dynamic light scattering and electrophoretic light scattering, respectively (Particle Sizing Systems, Port Richey, FL, USA).

Cell culture

Human MDA435 breast adenocarcinoma cells were stably transfected with the plasmid pEGFP-N1 (Clonetech Laboratories, Mountain View, CA, USA) to express enhanced green fluorescent protein (EGFP), and were further expanded and maintained in α-MEM supplemented with 10% fetal calf serum.

Animal models

All experiments were performed in accordance with the guidelines and regulations of the Animal Care Committee at the University Health Network (protocol number AUP1844). One million human MDA435 cells expressing EGFP were dispersed in either α-MEM or a 50% v/v mixture of α-MEM and Matrigel, and then injected (media only (Mat-) on the right and matrigel-media mixture (Mat+) on the left) into the inguinal mammary fat pads of nude mice using the subiliac lymph node as an injection landmark.

Optical imaging of nanoparticle retention in tumor

After successful tumor inoculation in the mammary fat pads of nude mice and sufficient tumor growth (up to about 200 mm^3 in volume after 3-4 weeks for Mat+tumors), 50 μL of QD-FEN was injected intratumorally in each of the bilateral tumors. Under continued isoflurane anesthesia, images were acquired of the ventral, left lateral, and right lateral aspects of the mice over time. At each time point, a bright field image was acquired, the EGFP-expressing tumors were imaged at 465 nm excitation and 540 nm emission, and the QD-FEN were imaged at 710 nm excitation and 840 nm emission using a Xenogen IVIS Spectrum (Caliper Life Sciences Inc., Hopkinton, MA, USA) whole animal imager. Image fluorescence was quantified by equalizing the fluorescence intensity range across all images and selecting a region of interest equal to the two-dimensional boundaries of the tumor.

Microbubble contrast enhanced sonography

Tumor locations were acquired using a Vevo 2100 high-frequency ultrasound imager (VisualSonics Inc., Toronto, Ontario, Canada) with mice under isoflurane anesthesia. DEFINITY® microbubbles (Lantheus Medical Imaging, North Billerica, MA, USA) were infused at 15 μl/min through a tail vein catheter. Once perfusion was noted, two high frequency pulses of 0.5 seconds were applied at default Vevo 2100 parameters to destroy the contrast agent in the imaged region, and the reperfusion of the tumor with microbubbles was recorded. The tumor was selected as a region of interest and the contrast enhancement of the region was plotted over time using Vevo® 2100 PC Workstation software (VisualSonics Inc., Toronto, Ontario, Canada). Curves were fitted to the data using NCSS v.17 (NCSS Inc, Kaysville, UH, USA) according to Signal Intensity = $\alpha(1-e^{-\beta t})$ as previously described for reperfusion kinetics analysis, where α = fractional vascular volume, $\alpha*\beta$ = volume flow rate, and t = time after microbubble ablation.[18]

Lymphatic flow optical imaging

In order to track the lymphatic flow from the base of the tail to beyond the axillary lymph nodes, 25 μL of 0.5% w/v ICG, a well characterized lymphatic tracer,[19,20] in 5% Dextrose solution was injected into the lateral tail subcutaneously, 1 cm caudally from the rectum, medial to the tail vein.[21] Images were acquired from the ventral aspect of animals using a Xenogen IVIS Spectrum (Caliper Life Sciences Inc., Hopkinton, MA, USA). Animals were euthanized by CO_2 30 minutes after ICG injection, followed by dissection to expose the subiliac and axillary lymph nodes, as well as the milk line lymphatic vessels. Images were acquired from the ventral aspect of animals using a Xenogen IVIS Spectrum as described above.

Histology

Following imaging procedures, mice were euthanized by CO_2 and the tumors with surrounding mammary fat pads, including lymph nodes, were quickly resected, formalin fixed, then embedded in paraffin. Sections were stained with hematoxylin and eosin (H&E) and 1:50 dilution of anti-CD31 antibody (Abcam Inc., Toronto, Canada) and visualized using biotinylated goat anti-rabbit antibody (1:500 dilution) (Vector Labs, Burlington, ON, Canada), or H&E and anti-LYVE1 antibodies to identify tumor and lymph node vasculature and lymphatics, respectively. Slides were scanned with an Aperio ScanScope XT (Aperio Technologies Inc., Vista, CA, USA) fitted with an Olympus 20×/0.75NA Plan Fluor lens, and processed using Aperio ImageScope v.9 (Aperio Technologies Inc., Vista, CA, USA).

Quantitative reverse transcription real-time PCR array of breast tumors

At necropsy, tumors were extracted aseptically, immersed in *RNAlater* Stabilization Reagent (Applied Bioscience), and stored according to manufacturer's instructions until extraction. Approximately 10 mg of tumor tissue was homogenized using a rotor stator homogenizer (IKA Ultra-Turrax T25 S1, Janke & Kunel, Staufen, Germany), and total RNA extracted in Trizol (Invitrogen). RNA was then isolated using RNeasy Mini Qiagen kit as per manufacturer's instructions. Initial quality and purity of the extracted RNA were determined using UV spectrophotometry based upon A260/A280 ratio. First strand cDNA synthesis was then performed using an RT^2 First Strand Kit (Qiagen) with an initial stock of 2 μg RNA in accordance with manufacturer's instructions. A human breast cancer RT^2 Profiler PCR array (384-well format – PAHS-131 E-1: Qiagen) was used, in accordance with the manufacturer's instruction and read using an ABI: 7900HT Real-time PCR Instrument (384-well block). The data were analyzed using the online RT^2 profiler PCR array data analysis software.

Statistical analysis

Values are expressed as the mean and standard deviation of three subjects. Regression analysis (Figure 2 and 5) and ANOVA with post-hoc Tukey tests (Figure 3) were performed using SPSS v17 (IBM, Chicago, IL, USA).

Results

Enhanced perfusion in Matrigel tumors over medium tumors

The perfusion of Mat− and Mat+tumors was assessed using microbubble contrast enhanced sonography.[18,22,23] As shown in Figure 1, at the same time post inoculation (i.e. 3-4 weeks), reperfusion in Mat+tumors was significantly faster compared to Mat− tumors. Frame captures with tumor vasculature highlight the accelerated reperfusion seen within Mat+tumors (Figure 1, *A*). Microbubble flow velocity was 0.36 s^{-1} in Mat+tumors and 0.12 s^{-1} in Mat− tumors. In addition, the cross-sectional perfusion, a measure of tumor vascular density,[22] was 7.52 cm^2/s in Mat+tumors, and 2.11 cm^2/s in Mat− tumors. While the rates of reperfusion were increased in Mat+tumors, the maximal contrast enhancement between the two tumor types was not significantly different (Figure 1, *C*).

Altered lymphatic function in Mat+versus Mat− tumors, which is independent of tumor size

A greater lymphatic flow rate in the collecting vessels is a marker for greater interstitial fluid exchange,[24] so lymphatic flow was determined by the interstitial injection of indocyanine green (ICG).[19,20] The flow of ICG from the injection site to the subiliac lymph node (SILN) was followed using live, whole animal fluorescent imaging (Figure 2, *A*). Mat+tumors exhibited greater lymphatic flow to the SILN than Mat− tumors, with flow rates of 3×10^7 ΔREU/min and 2×10^7 ΔREU/min, respectively, where REU are radiant efficiency units. In agreement with literature that Matrigel increases the rate of tumor xenograft growth,[1-3,5] in our bilaterial tumor model, the size of Mat− tumors were all significantly smaller than Mat+tumors at 3-4 weeks following inoculation (Figures 2 versus 2, *C*). To eliminate the possible influence of tumor size on tumor perfusion and lymphatic flow, Mat− tumors were allowed to develop until they were approximately equal in volume to the Mat+tumors (Figure 2, *D*). However the large

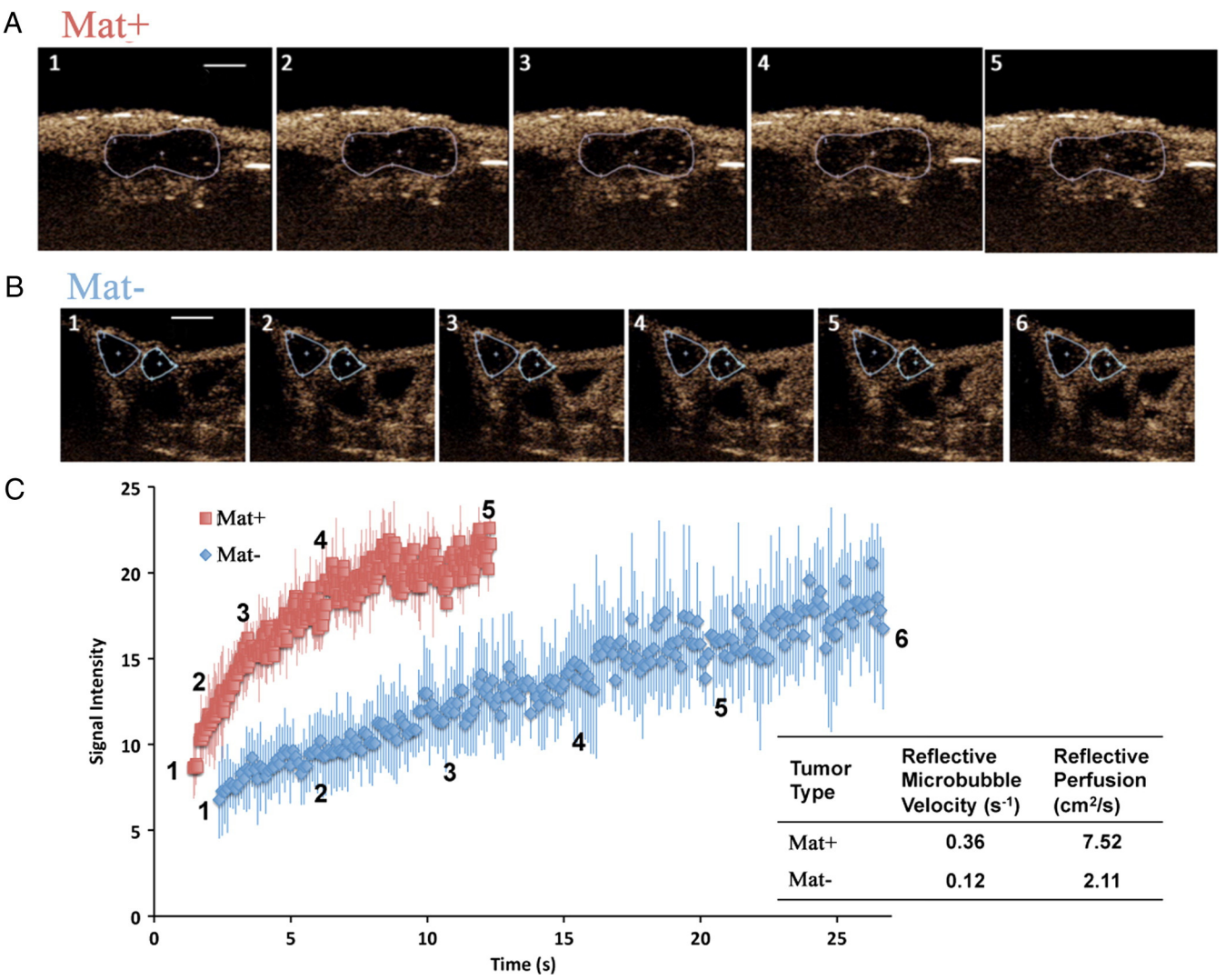

Figure 1. Sonographic images of tumor perfusion of Mat+ **(A)** and Mat− **(B)** MDA435 tumors and signal intensity vs. time plot **(C)**. The tumors are traced by white lines, indicating the regions of interest used to quantify contrast signal. Scale bars=3mm. The numbers on each curve match the numbered panels in A and B. The table inset presents the reflective microbubble velocity (s^{-1}) and reflective perfusion (cm^2/s) for Mat+ and Mat− tumors calculated from the average signal intensity vs. time curves. Each data point represents the mean±S.D. (n=3).

Mat− tumors did not exhibit significant changes in lymphatic flow rate with measured lymphatic flow rates of 2.1×10^7 ΔREU/min, similar to the smaller Mat− tumors (Figure 2, *F*).

Lymphatic anatomy was also examined under fluorescent imaging after the animals were euthanized and lymphatics from the base of the tail, along the milk line, to the axillary lymph node (ALN) were exposed (Figure 2, *B–E*). In the tumor-free (Figure 2, *E*), Mat- (Figure 2, *B*), and large Mat− (Figure 2, *D*) tumor-bearing animals, the milk line lymphatic vessel was a single, uniform vessel from SILN to ALN (Type-C[25]). However, in all Mat+tumor-bearing mice, this milk line vessel was bifurcated approximately half way between the SILN and ALN (Type-S[25]) (Figure 2, *G*). This bifurcation was not observed in any of the large Mat− tumor-bearing animals, however smaller lymphatic vessels were observed in the milk line lymphatic system proximal to the rostral aspect of the SILN (Figure 2, *D*). In all Mat− tumor-bearing mice, the tumor was observed only at the periphery of the SILN (Figure 2, *B* and *D*), where the Mat+tumors overgrew the SILN (Figure 2, *C*).

The lymph node morphology of Mat+tumor-bearing mice differs from that of Mat− tumor-bearing and tumor-free animals

Due to the different tumor growth patterns observed in the fluorescent imaging studies, the anatomical interaction of Mat− and Mat+tumors with the associated SILN was further investigated by sonography (Figure 3). In all animals bearing bilateral tumors, the Mat+tumor impinged on the associated SILN, resulting in a reduced cross-sectional area relative to SILN in tumor-free mice (Figure 3, *C*). Even in the mice bearing the large Mat− tumors (Figure 3, *B*), the size reduction of the SILN relative to other Mat− tumor-bearing animals, as well as the tumor-free SILN, was not significant.

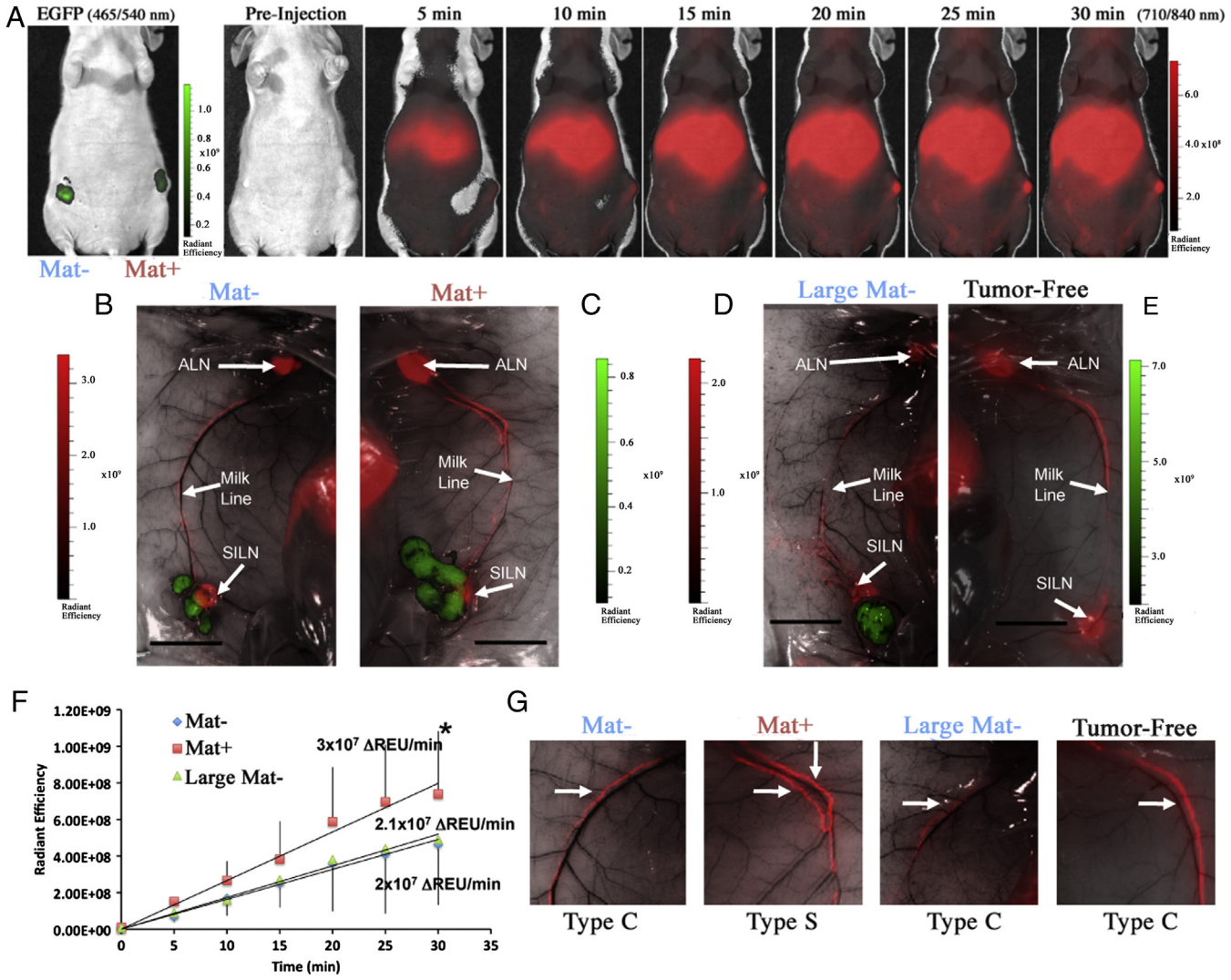

Figure 2. Representative optical images of a mouse bearing bilateral Mat− (left) and Mat+(right) tumors **(A)**, and *ex vivo* images of tissue dissected away of the skin revealing the tumor (green), SILN, milk line, and axillary lymph node (ALN) which were labeled with ICG in red for Mat− **(B)**, Mat+**(C)**, a large Mat− tumor **(D)**, and a tumor-free animal **(E)**. The lymphatic flow rate is shown in **(F)** for the Mat− (blue diamonds), Mat+(red squares), and large Mat− (green triangles) tumor groups. Scale bars in panels B to E represents 1 cm. The slope of the regression is indicated above each respective curve in units of change in fluorescence intensity (ΔREU) per unit time. Data points represent the mean±S.D. (n=3). A representative sample of the rostral portion of the milk line lymphatic vessels is shown in **(G)**. The alteration of the tumor-associated lymphatic of the Mat+tumor is indicated by two white arrows, clearly showing the bifurcation of the vessel. *Significantly different from the Mat− tumor and large Mat− tumor slope ($P<0.05$).

Differences in SILN and tumor vessel histology between Mat− and Mat+ tumors

To verify that the differences in the lymph node-associated growth pattern and the alterations in SILN anatomy observed between Mat+and Mat− tumors were not an artifact of the imaging modalities utilized, tumors and surrounding mammary fat pad (including the SILN) were examined histologically for the location and morphology of lymphatic and blood vessels using anti-Lyve1 (Figure 4, *A*, *C*, *E*, *G*, *I*, *K*, *M*, and *O*) and anti-CD31 (Figure 4, *B*, *D*, *F*, *H*, *J*, *L*, and *N*) antibodies, respectively.

The alteration of SILN morphology (LN) between Mat+(Figure 4, *A*) and Mat− (Figure 4, *C*) tumors was in agreement with the result seen using sonography (Figure 3), where the Mat+tumor-associated SILN appeared compressed relative to the elongated morphology seen in the Mat− (Figure 4, *E*) and tumor-free SILN (Figure 4, *G*). While the large Mat− tumor-associated SILN also exhibited the compressed state associated with Mat+tumors (Figure 4, *E*), histological differences in the lymphatic vessel morphology were observed between the large Mat− (Figure 4, *M*) and Mat+tumor-associated SILN (Figure 4, *I*). In the tumor-free- (Figure 4, *O*), Mat− (Figure 4, *K*), and large Mat− (Figure 4, *M*) tumor-associated SILN, the lymphatic vessels all exhibited a discernable luminal space. However in the Mat+tumor-associated SILN, the lymphatic vessels did not have a discernable lumen, indicative of vessel collapse (Figure 4, *I*). No differences were observed in the blood vessel morphology between any tumor-associated (Figure 4, *J*, *L*, and *N*) or tumor-free (Figure 4, *P*) SILN blood vessels.

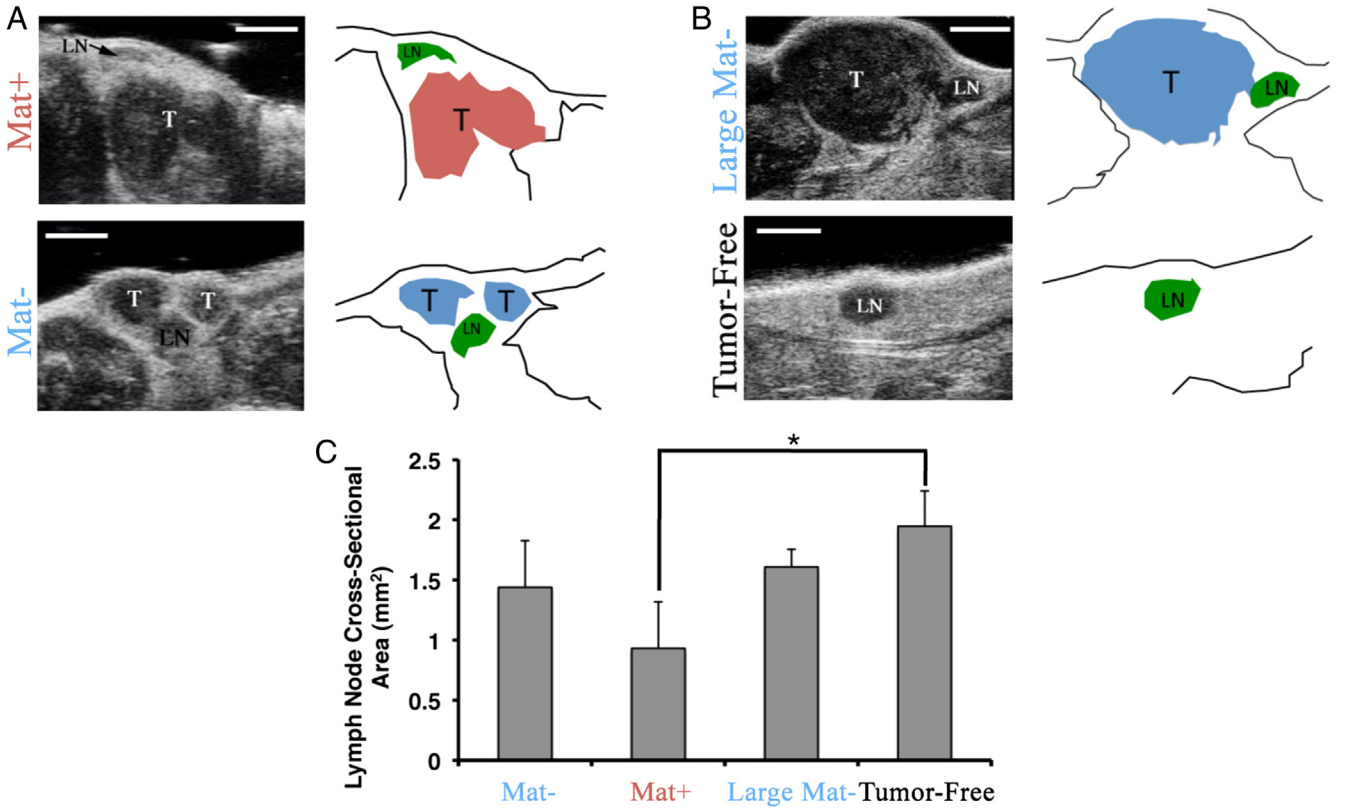

Figure 3. Ultrasonographic images of tumor and associated subiliac lymph nodes for a representative mouse bearing a Mat− tumor and a Mat+tumor bilaterally **(A)**, and a mouse bearing a large Mat− tumor and no tumor **(B)**. In **(A)** and **(B)**, the right two panels are line tracings of the ultrasound image showing the position of the tumors (T, red=Mat+and blue=Mat−) relative to the lymph node (LN, green). Scale bars=3 mm. The cross-sectional area of the lymph nodes was plotted for each of Mat−, Mat+, large Mat− tumor, and no tumor-bearing mice **(C)**. Bars represent the mean±S.D. (n=3). *Significantly smaller lymph node cross-sectional area relative to tumor-free mice ($P<0.05$).

The blood and lymph vessels that contribute to greater tumor-associated lymphatic flow and the greater tumor perfusion rates observed in Mat+tumors relative to Mat− tumors were examined histologically (Supplementary Figure 1). Tumor morphology was not observed to be different between Mat− tumors and Matr+tumors, as previously reported.[2,11] However only in the Mat+tumors were blood (Supplementary Figure 1, *B*) and lymphatic (Supplementary Figure 1, *C*) vessels present deep within the tumor tissue. Since these blood vessels contained red blood cells, they could be defined as functional.

Nanoparticles are poorly retained in Mat+tumors

Nanoparticle retention was assessed after intratumoral injection of quantum dot-loaded fatty ester nanoparticles (QD-FEN) into each tumor of mice bearing bilateral Mat− and Mat+tumors (Figure 5). Images were acquired from the ventral aspect (Figure 5, *A*), the left lateral aspect displaying the Mat+tumor (Figure 5, *B*), and the right lateral aspect displaying the Mat− tumor (Figure 5, *C*). Following intratumoral injection of QD-FEN, the fluorescence intensity of the quantum dots decreased more rapidly in Mat+tumors than in Mat− tumors (Figure 5, *B* versus *C*). In fact the QD-FEN-associated fluorescence in Mat+tumors decreased below background levels within 4 hours of administration, whereas the QD-FEN in Mat− tumors were still detectable beyond 6 hours of injection (Figure 5, *D*). These results indicate that the use of Matrigel in establishing xenograft human tumor models in mice significantly alters the retention of nanoparticles within the tumor, which could alter the efficacy of nanoparticles under evaluation as drug carriers.

Comparison of gene expression in breast tumors with Matrigel and that without Matrigel

The RNAs of Mat+or Mat− tumors were screened by the Human Breast Cancer RT^2 in which there were 84 key gene expressions commonly involved in the mis-regulation of signal transduction or other biological process in human breast cancer cell lines. Of 84 gene mRNAs that were profiled, only 7 genes were found to exhibit over two-fold differences between Mat+and Mat− tumors, namely cyclin A1 (CCNA1, +2.8), cyclin-dependent kinase inhibitor 1C (CDKNIC,−3.6), cystatin M (CST6,−2.1), estrogen receptor b (ESR2,−2.9), Gli1(GLI1,−2.1), matrix metalloproteinase 2 (MMP2,−5.2) and apoptosis-associated speck-like protein containing a CARD (PYCARD,−2.8) (Table 1). However, because the average threshold cycle of these gens is relatively high (>30) and thereby their relative expression levels are low, the data could not show statistically significant difference between

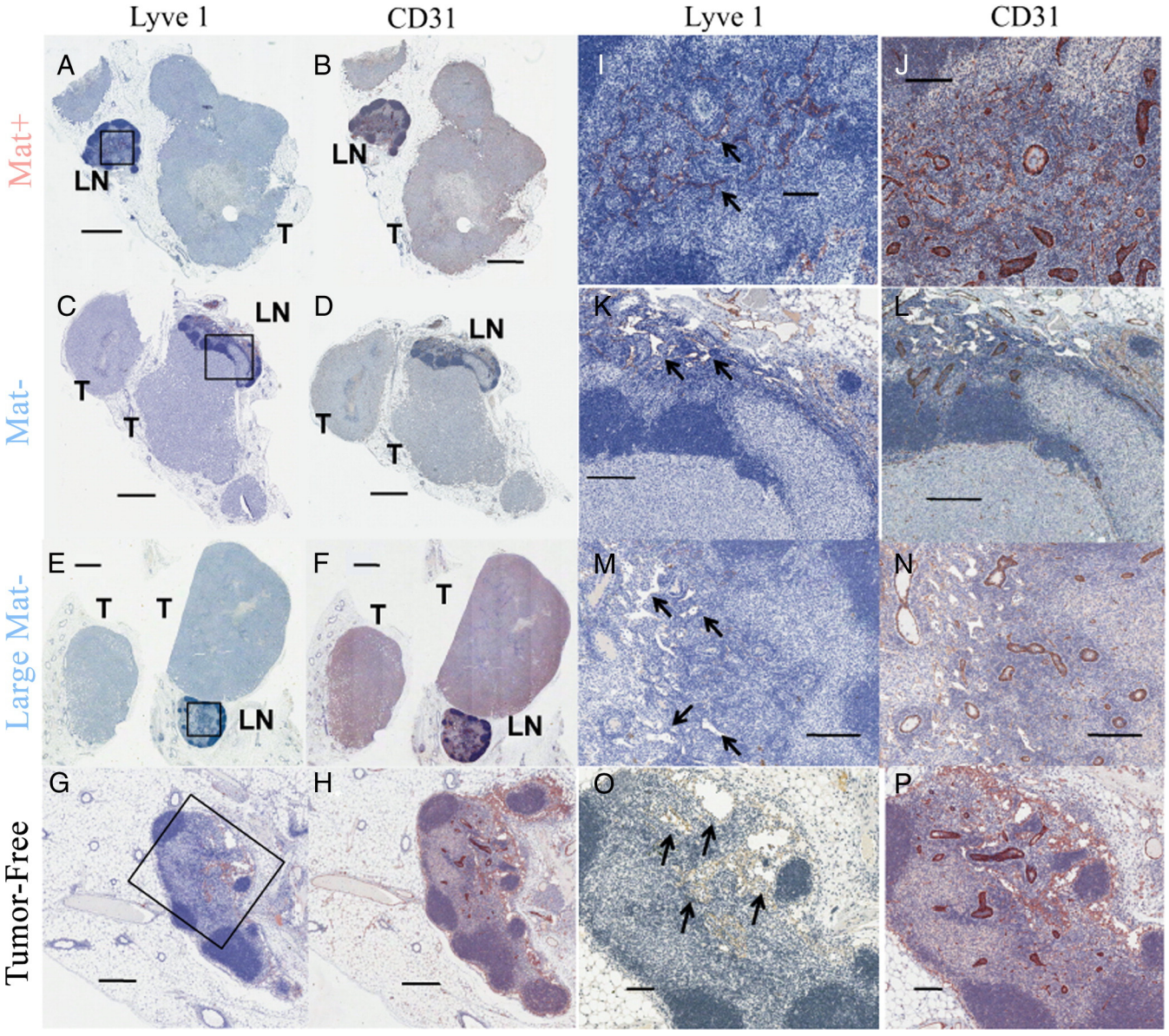

Figure 4. Histology of whole tumors from Mat+(**A** and **B**), Mat− (**B** and **D**), large Mat− tumors (**E** and **F**), and tumor-free lymph node (**G** and **H**). The samples were stained with H&E in combination with either anti-Lyve 1 antibodies to demarcate lymphatic vessels (**A**, **C**, **E**, and **G**), or anti-CD31 antibodies to indicate blood vessels (**B**, **D**, **F**, and **H**). T: tumor tissue, LN: lymph node. The solid boxes in A, C, E, and G represent the areas enlarged in panels I–P. Lymph node histology can be seen for Mat+(**I** and **J**), Mat− (**K** and **L**), large Mat− (**M** and **N**), and tumor-free tissue (**O** and **P**). Lymph node lymphatic vessels stained by anti-Lyve-1 antibodies are indicated by black arrows (**I**, **K**, **M**, and **O**), while lymph node blood vessels were labeled by anti-CD31 antibodies (**J**, **L**, **N**, and **P**). Scale bars in A–F are 1 mm, G and H are 250 μm, and I to P are 100 μm.

Mat+and Mat− tumors. A more extensive study with large sample sizes is required to delineate the gene profile changes, which is beyond the scope of this paper.

Discussion

The effect of Matrigel on tumor pathophysiology has been evaluated here in a bilateral orthotopic mouse model of human breast adenocarcinoma established with Matrigel (Mat+) or without Matrigel (Mat−) during tumor inoculation. The efficacy of nanoparticle drug carriers largely depends on their tumor accumulation, which is determined by their permeation and retention in tumors. Since permeation and retention are not independent processes, intratumoral injection of nanoparticles was utilized in this work to avoid the possibility of Matrigel-induced variations in nanoparticle permeation between Mat+tumors and Mat− tumors. Intratumoral injection could control the amount of nanoparticles introduced into each tumor type, permitting the specific effect of Matrigel on nanoparticle retention to be evaluated separately.

While unique tumor pathophysiology enhances both accumulation and retention as described by the EPR effect,[8,9] two Matrigel-associated alterations of tumor pathophysiology

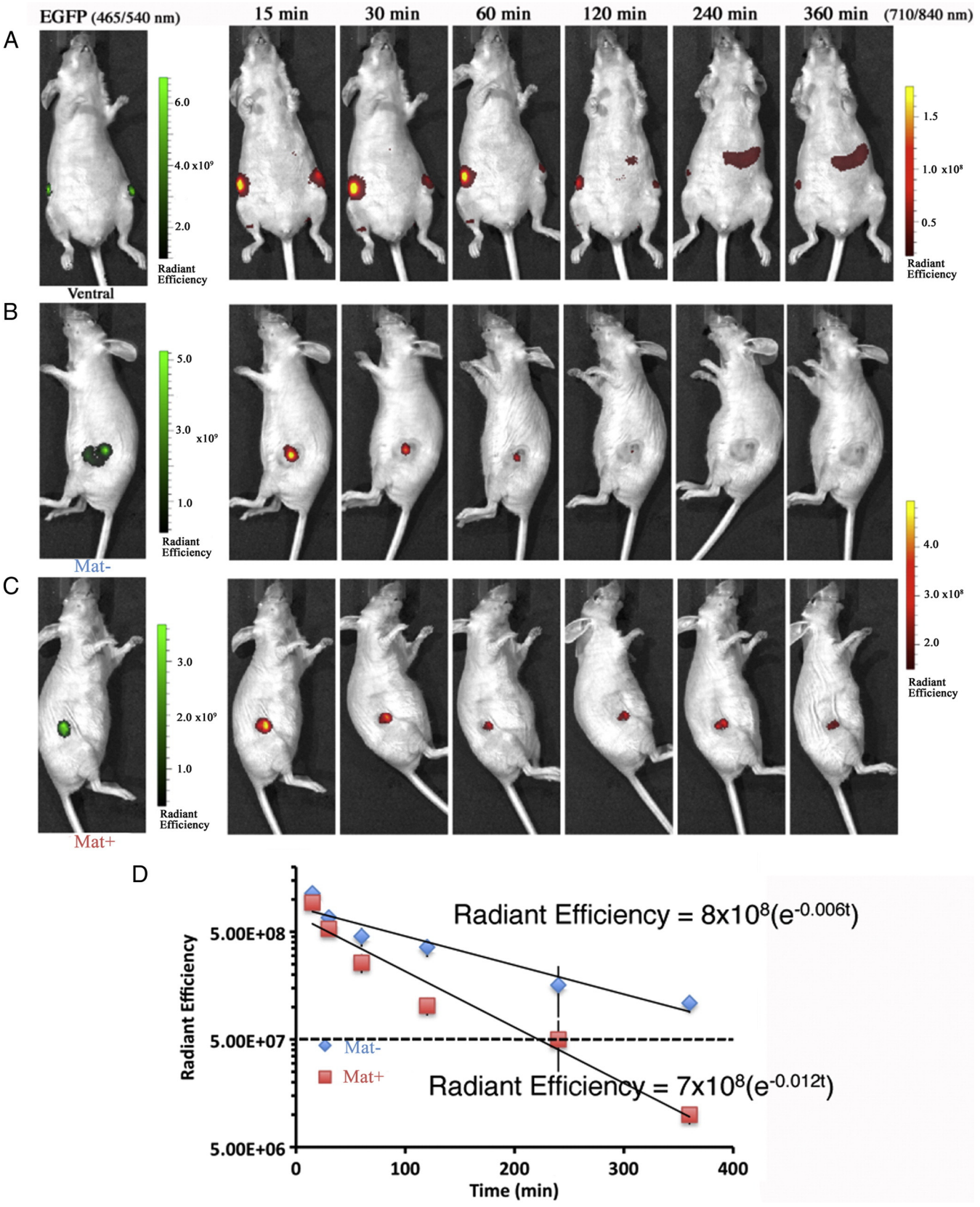

Figure 5. Whole animal fluorescent images of representative mice at different times after intratumoral administration of nanoparticles acquired serially from the ventral **(A)**, left lateral the Mat+tumor **(B)**, and right lateral, the Mat− tumor **(C)** aspects. **(D)** A plot of the fluorescence intensity levels over time confirms the significantly poorer retention of nanoparticles in Mat+(red squares) versus Mat− (blue diamonds) tumors ($P<0.05$). The broken line represents the background fluorescence intensity. Each point represents the mean±S.D. (n=3).

Table 1
The results of gene mRNAs profiled by the Human Breast Cancer RT^2 (n=3, no statistically significant difference).

Gene name	Gene symbol	Fold difference	Gene function
Cyclin A1	CCNA1	2.8	Promitotic signal through Rb/E2F transcription
Cyclin-dependent kinase inhibitor 1C	CDKN1C	−3.6	Antimitotic signal, inhibiting E2F transcription and downregulating Cyclin A1 expression
Cystatin M	CST6	−2.1	Tumor suppressor gene, inhibiting lysosomal cysteine proteases to suppress proliferation, invasion, and migration of tumor cells
Estrogen receptor B	ESR2	−2.9	Antimitotic signal, preventing HIF-1α transcription of growth genes
Gli1	GLI1	−2.1	Tumor promoter gene through downstream activator in hedgehog signaling pathway and activation of tumor growth and survival signals
Matrix metalloproteinase 2	MMP2	−5.2	Involved in stromal degradation to promote metastasis
Apoptosis-associated speck-like protein containing a CARD	PYCARD	−2.8	Pro-apoptotic signal, mediating the activation of NF-κB to promote caspase activation

The difference between Mat+and Mat− tumors was calculated as ratios of corresponding gene expression levels of Mat+tumors to those of Mat− tumors (n=3, no statistically significant difference between Mat+and Mat− tumors).

revealed in this work could oppose the EPR effect: (1) enhanced tumor vascular perfusion rates (Figure 1); and (2) enhanced lymphatic flow rates (Figure 2). These effects resulted in the faster clearance of nanoparticles from Mat+tumors (Figure 5), an effect attributable to Matrigel but not tumor size, as size-matched Mat− tumors did not show the same physiological alterations. Enhanced vascularity was evidenced in Mat+tumors by a greater cross-sectional perfusion, and by the presence of large, functional blood vessels identified by CD31 immunohistochemistry within the tumor (Figure 5, *B*). In contrast, none of the Mat− tumors, regardless of size, contained vasculation towards the core of the tumor (Figure 5, *C*).

Greater blood flow to tumors can be both beneficial and detrimental to the EPR effect on nanoparticle accumulation in tumor. With enhanced blood flow, the accessibility of nanoparticles to tumor tissue increases according to Starling's law[26] (Figure 6), because higher microvascular flow increases microvascular pressure (p_v), favoring the flux (J_v) of fluid and suspended nanoparticles through leaky tumor vasculature. Nevertheless, it has been demonstrated previously that nanoparticles can exit the tumor by the vascular system just as readily as they diffuse into the tumor tissue.[27,28] High tumor perfusion rates can enhance nanoparticle clearance by (1) reducing the residence time of nanoparticles in tumor vasculature and the probability of extravasation; and (2) increasing the flux of fluid from the blood vessel into the tumor, which raises the interstitial fluid pressure (p_i) and creates a back-pressure on the particles, preventing their extravasation and encouraging their circulation in the blood stream (Figure 6).[29,30]

Higher interstitial fluid pressure, which is a hallmark of solid tumors, would result in convective fluid flow from the core of the tumor down pressure gradients to the peritumoral tissue that contains the lymphatic vessels.[29–31] Since the lymphatic system drains interstitial fluid,[24] and since enhanced convective flow would increase local lymphatic flow rates, monitoring lymphatic flow rates becomes a surrogate marker for enhanced convective fluid flow. Therefore, the enhanced lymphatic flow rates observed in Mat+tumor-associated lymphatics may be the result of elevated interstitial fluid pressures and enhanced convective fluid flow due to alterations of the tumor stroma caused by Matrigel.

Tumor stroma is defined by collagen, but the functional aspects, such as fluid balance, are regulated by biological mediators that interact with the collagen framework: namely proteoglycans and tissue fibroblasts.[24,26] Proteoglycans establish interstitial volume by increasing the osmotic pressure of the stroma through anionic glycosaminoglycans.[24] Fibroblasts directly exert tension on collagen under stimulation by platelet derived growth factor and transforming growth factor-β, limiting the swelling pressure induced by proteoglycans and regulating interstitial fluid pressure.[26] Matrigel contributes proteoglycans to the artificial tumor stroma it forms,[2] which can elevate the osmotic pressure (π_i) within the tumor. In addition, Matrigel, consisting of platelet derived growth factor and transforming growth factor-β,[2] can promote fibroblast contraction of the collagen framework of the tumor.

Due to the glycosaminoglycan and proteoglycan content of Matrigel, the π_i of Mat+tumors may be increased, which, according to Starling's Law, could increase fluid flow from the vasculature to the tumor interstitium.[26,29] Since the observed increase in Mat+tumor perfusion (Figure 1) would increase the microvascular pressure (p_v), an increase in both p_v and π_i would increase the fluid flux (J_v) into the tumor and further raise p_i (Figure 6). To balance the increase in p_i, convective fluid flow from the tumor interstitium to the peritumoral region would increase, ultimately draining into tumor-associated and peritumoral lymphatics. This increased convective fluid flow would carry the nanoparticles out of the Mat+tumor at a greater rate than from the Mat− tumor, hastening the clearance of nanoparticles from the tumor tissue. Thus, it is possible that the increased tumor perfusion rates observed in Mat+tumors resulted in the rapid nanoparticle leakage from this tumor type (Figure 5, *B*). Of future interest is the effect of Mat+on the accumulation and ultimately changes in the therapeutic efficacy of nanoparticles in tumor tissue following intravenous administration of nanoparticles to Mat+tumor-bearing mice.

In agreement with previous reports,[2] no alteration to Mat+tumor cell morphology was observed (Supplementary Figure 1, *D* versus *H* versus *L*). However it has been demonstrated here that Matrigel influences tumor vascular and lymphatic access, impacting physiological parameters critical to nanoparticulate drug delivery to tumors. For the

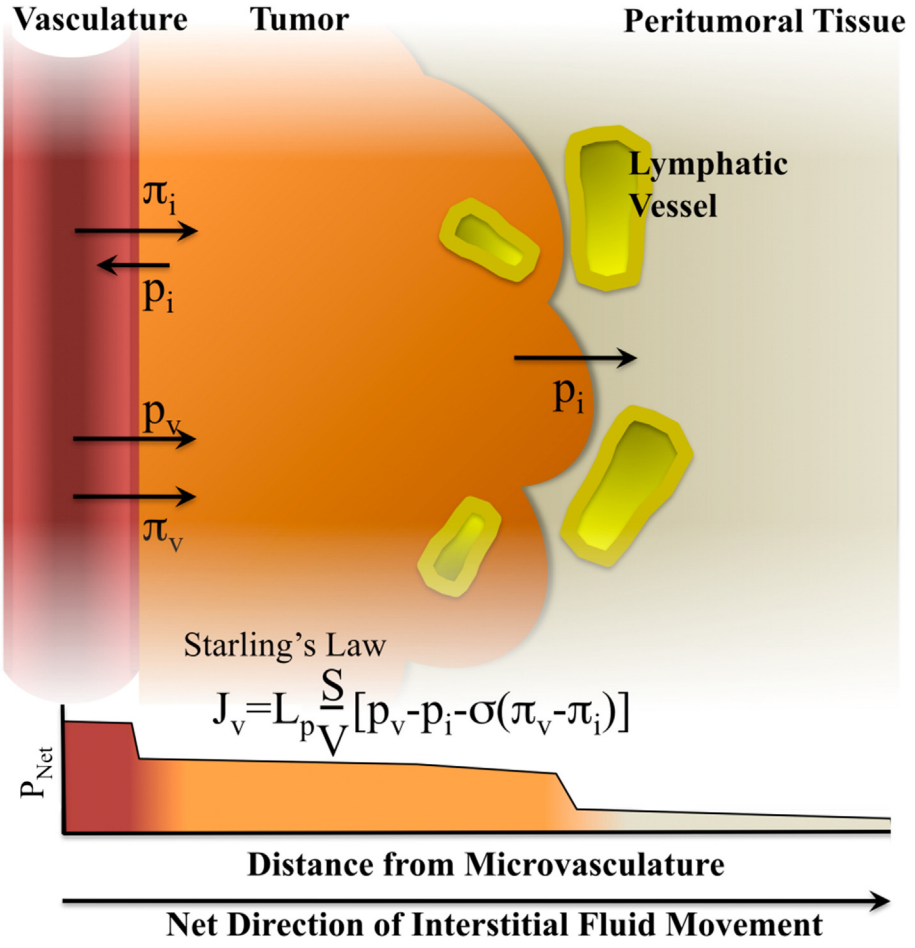

Figure 6. Schematic illustration of proposed mechanism of interstitial fluid flow in relation to tumor perfusion. Fluid efflux from the vasculature (J_v) is defined by the balance of fluid pressures remove inner brackets and osmotic pressures (π_v and π_i) in the vasculature and interstitial space, respectively, according to Starling's Law. The arrows represent the fluid flow under influence of the indicated pressures. The high p_v and low π_v, coupled with the high π_i and low p_i results in a net J_v out of the vasculature (red) and into the tumor (orange). The abrupt interstitial pressure (P_{Net}) drop in the peritumoral interstitium (brown), relative to the tumor interstitium, induces a net convective fluid flow from the tumor to the peritumoral tissue. At the tumor periphery, interstitial fluid is collected in the lymphatic vessels (yellow), reinforcing the interstitial convective fluid flow towards the peritumoral tissue. Starling's Law also contains L_p: hydraulic conductivity of the vascular wall; S/V: surface area to volume ratio of the microvascular vessel; σ: average osmotic reflection coefficient for plasma proteins.

first time, the bifurcation of the collecting lymphatic vessel unique to the Mat+tumor-associated lymphatics was observed (Figure 2, *G*), a phenomenon which has been noted clinically in a minority (~20%) of patients with breast cancer.[25] Though the clinical significance of single (Type-C) or bifurcated (Type-S) lymphatic vessels is not yet known,[25] Matrigel could be employed to induce animal models with this same altered lymphatic architecture.

In conclusion, Matrigel alters the perfusion and associated lymphatic physiology and anatomy of xenograft breast tumors. Enhanced tumor perfusion and lymphatic flow rates, coupled with deeper blood and lymph vessel penetration may have resulted in the poorer retention of nanoparticles in Mat+tumors. The associated pathophysiological alterations could have detrimental implications of poor nanoparticle retention and limited nanomedicine anticancer efficacy as the EPR effect that allows for passive tumor targeting may be diminished. Not only do the results presented here necessitate the careful evaluation of the use of Matrigel in tumor models assisting nanoparticulate drug carrier design, but also demonstrate the importance of tumor interstitial biology and architecture on nanomedicines.

Acknowledgments

The authors gratefully acknowledge STTARR for assistance with the ultrasound and fluorescent imaging modalities.

Appendix A. Supplementary data

Supplementary data to this article can be found online at http://dx.doi.org/10.1016/j.nano.2013.01.005.

References

1. Benton G, Kleinman HK, George J, Arnaoutova I. Multiple uses of basement membrane-like matrix (BME/Matrigel) in vitro and in vivo with cancer cells. *Int J Cancer* 2010.

2. Fridman R, Kibbey MC, Royce LS, Zain M, Sweeney M, Jicha DL, et al. Enhanced tumor growth of both primary and established human and murine tumor cells in athymic mice after coinjection with Matrigel. *J Natl Cancer Inst* 1991;**83**:769-74.
3. Kleinman HK, Martin GR. Matrigel: basement membrane matrix with biological activity. *Semin Cancer Biol* 2005;**15**:378-86.
4. Liotta LA, Rao CN, Wewer UM. Biochemical interactions of tumor cells with the basement membrane. *Annu Rev Biochem* 1986;**55**:1037-57.
5. Terranova VP, Williams JE, Liotta LA, Martin GR. Modulation of the metastatic activity of melanoma cells by laminin and fibronectin. *Science* 1984;**226**:982-5.
6. Vaillant F, Lindeman GJ, Visvader JE. Jekyll or Hyde: does Matrigel provide a more or less physiological environment in mammary repopulating assays? *Breast Cancer Res* 2011;**13**:108.
7. Torchilin VP. Passive and active drug targeting: drug delivery to tumors as an example. *Handb Exp Pharmacol* 20103–53.
8. Maeda H, Wu J, Sawa T, Matsumura Y, Hori K. Tumor vascular permeability and the EPR effect in macromolecular therapeutics: a review. *J Control Release* 2000;**65**:271-84.
9. Maeda H. The enhanced permeability and retention (EPR) effect in tumor vasculature: the key role of tumor-selective macromolecular drug targeting. *Adv Enzyme Regul* 2001;**41**:189-207.
10. Wang M, Thanou M. Targeting nanoparticles to cancer. *Pharmacol Res* 2010;**62**:90-9.
11. Kim WH, Jun SH, Kibbey MC, Thompson EW, Kleinman HK. Expression of beta 1 integrin in laminin-adhesion-selected human colon cancer cell lines of varying tumorigenicity. *Invasion Metastasis* 1994; **14**:147-55.
12. Huang NF, Yu J, Sievers R, Li S, Lee RJ. Injectable biopolymers enhance angiogenesis after myocardial infarction. *Tissue Eng* 2005;**11**:1860-6.
13. Ou L, Li W, Zhang Y, Wang W, Liu J, Sorg H, et al. Intracardiac injection of matrigel induces stem cell recruitment and improves cardiac functions in a rat myocardial infarction model. *J Cell Mol Med* 2010.
14. Hoshi M, Williams M, Kishimoto Y. Esterification of fatty acids at room temperature by chloroform-methanolic HCl-cupric acetate. *J Lipid Res* 1973;**14**:599-601.
15. Evans CM, Guo L, Peterson JJ, Maccagnano-Zacher S, Krauss TD. Ultrabright PbSe magic-sized clusters. *Nano Lett* 2008;**8**:2896-9.
16. Shuhendler AJ, Prasad P, Chan HK, Gordijo CR, Soroushian B, Kolios M, et al. Hybrid quantum dot-fatty ester stealth nanoparticles: toward clinically relevant in vivo optical imaging of deep tissue. *ACS Nano* 2011;**5**:1958-66.
17. Shuhendler AJ, Prasad P, Leung M, Rauth AM, Dacosta RS, Wu XY. A novel solid lipid nanoparticle formulation for active targeting to tumor alpha(v) beta(3) integrin receptors reveals cyclic RGD as a double-edged sword. *Adv Healthc Mater* 2012;**1**:600-8.
18. Cosgrove D, Eckersley R, Blomley M, Harvey C. Quantification of blood flow. *Eur Radiol* 2001;**11**:1338-44.
19. Kwon S, Sevick-Muraca EM. Noninvasive quantitative imaging of lymph function in mice. *Lymphat Res Biol* 2007;**5**:219-31.
20. Unno N, Inuzuka K, Suzuki M, Yamamoto N, Sagara D, Nishiyama M, et al. Preliminary experience with a novel fluorescence lymphography using indocyanine green in patients with secondary lymphedema. *J Vasc Surg* 2007;**45**:1016-21.
21. Harrell MI, Iritani BM, Ruddell A. Lymph node mapping in the mouse. *J Immunol Methods* 2008;**332**:170-4.
22. Niermann KJ, Fleischer AC, Huamani J, Yankeelov TE, Kim DW, Wilson WD, et al. Measuring tumor perfusion in control and treated murine tumors: correlation of microbubble contrast-enhanced sonography to dynamic contrast-enhanced magnetic resonance imaging and fluorodeoxyglucose positron emission tomography. *J Ultrasound Med* 2007;**26**:749-56.
23. Yankeelov TE, Niermann KJ, Huamani J, Kim DW, Quarles CC, Fleischer AC, et al. Correlation between estimates of tumor perfusion from microbubble contrast-enhanced sonography and dynamic contrast-enhanced magnetic resonance imaging. *J Ultrasound Med* 2006;**25**: 487-97.
24. Swartz MA. The physiology of the lymphatic system. *Adv Drug Deliv Rev* 2001;**50**:3-20.
25. Hojo T, Nagao T, Kikuyama M, Akashi S, Kinoshita T. Evaluation of sentinel node biopsy by combined fluorescent and dye method and lymph flow for breast cancer. *Breast* 2010;**19**:210-3.
26. Heldin CH, Rubin K, Pietras K, Ostman A. High interstitial fluid pressure – an obstacle in cancer therapy. *Nat Rev Cancer* 2004;**4**:806-13.
27. Dreher MR, Liu W, Michelich CR, Dewhirst MW, Yuan F, Chilkoti A. Tumor vascular permeability, accumulation, and penetration of macromolecular drug carriers. *J Natl Cancer Inst* 2006;**98**:335-44.
28. Lee H, Fonge H, Hoang B, Reilly RM, Allen C. The effects of particle size and molecular targeting on the intratumoral and subcellular distribution of polymeric nanoparticles. *Mol Pharm* 2010;**7**:1195-208.
29. Jain RK. Determinants of tumor blood flow: a review. *Cancer Res* 1988;**48**:2641-58.
30. Jain RK. Delivery of molecular and cellular medicine to solid tumors. *J Control Release* 1998;**53**:49-67.
31. Boucher Y, Baxter LT, Jain RK. Interstitial pressure gradients in tissue-isolated and subcutaneous tumors: implications for therapy. *Cancer Res* 1990;**50**:4478-84.